Available online at www.sciencedirect.com

ScienceDirect

Ceramics International 40 (2014) 3041–3051

CERAMICS INTERNATIONAL

www.elsevier.com/locate/ceramint

Permeability and dynamic elastic moduli of controlled porosity ultra-precision aerostatic structures

I.S. Durazo-Cardenas*, J. Corbett, D.J. Stephenson

Cranfield University, Cranfield, Bedfordshire MK43 0AL, United Kingdom

Received 13 May 2013; received in revised form 10 September 2013; accepted 2 October 2013
Available online 11 October 2013

Abstract

Porous ceramic aerostatic bearings enable precise and smooth motion and improved stiffness compared with widely used orifice restrictor bearings. However, the processing techniques so far used are too complex or rely in lowering the sintering temperature to increase fluid flow.

Preferred combinations of fine-grade alumina powders and starch granules were used to produce quality porous structures using fixed processing parameters. Component shrinkage, permeability, pore size and elastic properties were comprehensively characterised as a function of porosity.

The new porous ceramic structures exhibited controllable and reproducible permeability and modulus, within the range required for ultra-precision porous aerostatic applications.

Keywords: B. Porosity; C. Mechanical properties; D. Al_2O_3; E. Porous bearings; Permeability

1. Introduction

Porous ceramics are typically used in a variety of applications such as filters, high temperature insulators and sensors. [1,2]. They have also been developed for high-precision porous thrust aerostatic-bearings applications [3,4]. These bearings enable precise and smooth non-contact relative motion of machine components. Clean compressed air is supplied to the bearing clearance through the extremely large number of integrated restrictors in the porous wall. As a result, the bearing fluid-film pressure distribution is improved. This in turn results in an enhanced load carrying capacity and stiffness, higher than that of widely used discrete orifice-restrictor bearings. Porous aerostatic bearings can potentially be used in the manufacture of highly value added components such as precision optics, coordinate measuring machines (CMMs), MEMS, replication drums, etc.

Further advantages of ceramics as bearing material are their low coefficient of expansion, long term dimensional stability and stiffness over a wide range of temperatures. In addition, ceramics can be machined without pore smearing [5]. In addition to more traditional porous bearing materials such as bronze, porous graphite and ceramics, high strength porous cementitious composites have been recently explored [6].

Precision porous guideway thrust bearings may have the shape of a simple disc or pad. These bearings enable precise and smooth linear motion. The accuracy-demanding applications in which they are used require well defined and controlled permeability coupled with good mechanical properties. Based on analytical models, Kwan [5] calculated the permeability and Young's modulus requirements for ceramic aerostatic porous pads. His study showed the permeability required for high stiffness ranged from 3.13×10^{-15} to 8.44×10^{-14} m^2. A desirable value of Young's modulus for the porous material was estimated at 102 GPa to prevent excessive deflection under pressure. These values were used as targets at the start of the research.

Manufacture methods that have been previously used were either too complex [4] to be widely employed, or relied in lowering the sintering temperature to increase fluid flow [3]. The latter is widely known to result in reduced mechanical

*Corresponding author. Tel: +44 12 3475 0111.
E-mail address: i.s.durazocardenas@cranfield.ac.uk (I.S. Durazo-Cardenas).

0272-8842/$ - see front matter © 2013 Elsevier Ltd and Techna Group S.r.l. All rights reserved.
http://dx.doi.org/10.1016/j.ceramint.2013.10.003

properties. Kwan [4,5] first developed an alumina porous ceramic material suitable for high precision aerostatic bearings. A multi-layer approach was used combining several ceramic processing routes. The first layer was a 23 μm alumina powder substrate that provided the bulk of the mechanical properties. This was fabricated by capsule free Hot Isostatic Pressing (HIPing). The second layer was a fine pressure restricting layer made form 0.45 μm alumina powder fabricated by slip-casting. A tape-cast strip made with 0.45 μm alumina placed in-between the 2 layers was used for bonding by hot pressing. Roach [3] investigated several ceramics manufacturing routes in order to simplify the manufacturing method proposed by Kwan [5]. He focused his work on the ceramic injection moulding and slip casting techniques, primarily using sub-micron alumina powders.

The authors have recently published a paper [7] that dealt with porous ceramic hydrostatic journal bearings for rotational motion, manufactured by the starch consolidation technique (SC). These bearings had hollow cylinder geometry and used oil or water as fluid. Their permeability, porosity and pore size were all expressed as a function of the alumina size and volume per cent of starch. In difference to those, aerostatic guideway pad bearings, provide virtually frictionless linear motion using air as fluid film. The compressibility of air often means that the bearing gap is usually smaller (typically ≤ 10 μm) to avoid instability. As a result, the permeability requirement for optimum performance differs slightly from that of porous hydrostatic bearings.

In the present work, the effect of porosity on the permeability, microstructure and pore size on a range of disc-shaped aerostatic-pad starch consolidation (SC) specimens has been examined. Young's and shear moduli have been characterised for the first time for SC porous bearings.

2. Theoretical

2.1. Dimensional shrinkage and process densification

The sintering process is generally accompanied by some degree of shrinkage. From a bearing pad processing point of view, it is important to account for this to produce usable porous bearing castings with controlled dimensions. Shrinkage S is defined as the change in compact length from the green dimension Δ_L divided by its initial dimension L_0 [8].

$$S = \frac{\Delta_L}{L_0} \tag{1}$$

The density of typical sintered compacts can be calculated from initial values of the green density and the amount of shrinkage by [8]

$$\rho_s = \frac{\rho_g}{\left(\frac{1-\Delta L}{L_0}\right)^3} \tag{2}$$

where ρ_s is the sintered density and ρ_g is the green density.

2.2. Permeability

The permeability of the porous wall profoundly influences the overall bearing performance [9]. Other design parameters such as the bearing gap, the bearing dimensions and the fluid supply pressure also play a significant part [10].

Bearing permeability is generally expressed using Darcy's law [9]. This describes the flow of fluids through porous materials at relatively low velocity, where only viscous factors are prevalent. The equation used to derive the viscous permeability coefficient ψ can be written [11]:

$$\frac{\Delta_p}{e} = \frac{Q\,\eta}{A\,\psi} \tag{3}$$

At higher flow rates, inertial effects become significant and Forchheimer's equation is used for the determination of the viscous ψ and inertial permeability ψ_i coefficients [11]:

$$\frac{\Delta_p}{e} = \frac{Q\,\eta}{A\,\psi} + \frac{Q^2\,\rho}{A^2\,\psi_i} \tag{4}$$

where A is the area of the porous material normal to the direction of the fluid flow in m^2, Δp is the pressure drop in N/m^2, e is the thickness of the test piece in m, Q is the volume flow rate in m^3/s, η is the absolute dynamic viscosity in Ns/m^2, ρ is the density of the test fluid is kg/m^3, ψ is the viscous permeability coefficient in m^2 and ψ_i is the inertial permeability coefficient in m^2. Eqs. (3) and (4) describe the relationship between pressure drop Δp and volume flow rate Q.

Permeability has been traditionally expressed as a function of porosity and particle size [12] and also the porosity and mean pore size [13]. Permeability of SC porous structures was first characterised by Vasconcelos et al. [14], as a function of their mean pore size, using a power law form equation:

$$\Psi = kd^a \tag{5}$$

where k and a are the empirical constants and d is the mean pore size.

For SC porous hydrostatic journal bearings, permeability has been expressed as an exponential function of the volume per cent of starch for each alumina size used [7]:

$$\Psi = ke^{as} \tag{6}$$

where s is the starch volumetric constant.

2.3. Young's modulus requirement

Estimation of Young's modulus requirement of a porous ceramic pad bearing has been previously [5] calculated using [15]:

$$\delta_c = -0.07\frac{\Delta p r_p^4}{X z_p{}^3}12(1-v^2) \tag{7}$$

where δ_c is the deflection at the centre of a simply supported porous pad. Δp is the pressure drop across the bearing. X is the modulus of elasticity, r_p is the radius of the pad, z_p is the thickness and v is Poisson's ratio. Kwan's [5] ultra-precision

Table 1
Raw materials used in the slips formulation for the manufacture of porous ceramic hydrostatic bearings.

Material	Supplier	Median particle size (μm)	Surface area (m^2/g)
Maize Starch 03401	CERESTAR UK Ltd	10–20	–
Dispersant Dispex A40	Allied colloids ltd	–	–
Al_2O_3 (RA 45E)	ALCAN	0.45	7.5
Al_2O_3 (RA 7)	ALCAN	1.1	2.9
Al_2O_3 (RA 10)	ALCAN	2.1	2.2
Al_2O_3 (RA 15)	ALCAN	2.7	3.7
Al_2O_3 (RA 12)	ALCAN	4	1.8
De-ionised water	–	–	–

bearing Young's modulus requirement of 102 GPa, was obtained assuming a maximum deflection of 1 μm, i.e. 10% of design bearing gap. Δp was of 0.17 MPa, thickness 6 mm and a υ of 0.15. However, it is acknowledged that Young's modulus requirement may vary with the choice of design and operational parameters. For ultra-precision applications, the magnitude of δ_c would be of considerable effect due to the size of bearing gaps often employed (≤ 10 μm).

Young's modulus is critical to the structural integrity of the aerostatic porous pad due to the supply pressure and loading. Nevertheless, the shear modulus is also important as these bearings are often designed to provide linear motion under loading.

2.4. Elastic moduli and porosity relationship

An in-depth analytical review of the porosity–elasticity relations for porous ceramics has been presented by Pabst et al. [16]. Researchers have generally correlated porosity with the observed elastic constants. Published works typically use either a power law function or an exponential form equation to describe these relationships. One of the most acknowledged analyses is the model proposed by Phani et al. [17], which is based on the theory of elasticity of a continuum with pores as a second phase:

$$X = X_0\left(1 - \frac{\zeta}{\zeta_{cr}}\right)^a \tag{8}$$

where X is the modulus of elasticity, X_0 is the full dense material modulus of elasticity, a is a constant, ζ is the fractional porosity and ζ_{cr} is the critical porosity at which X becomes zero. Wagh et al. [18] argued that fitted experimental data yields $\zeta_{cr}=1$ resulting in a simplified model:

$$X = X_0(1-\xi)^a \tag{9}$$

Other authors such as Duckworth [19] and Spriggs [20] used an exponential function:

$$X = X_0 e^{-b\xi} \tag{10}$$

where b is an empirical constant.

Recently, Zivcova et al. [21] proposed a new relationship observing a good correlation of the moduli with porosity for ceramics made by the starch consolidation technique:

$$X = X_0\left[\frac{(1-\xi)^2}{1+\xi}\right] \tag{11}$$

Shear modulus is generally expected to observe a similar porosity dependence function to that of the elastic modulus, although this may show different numerical constants [21].

3. Materials and methods

3.1. Specimen preparation

Specimens were prepared by the SC technique [22–24]. In agreement with previous research [7], similar ceramic slips were prepared with mono-sized alumina powders (Alcan Chemicals Europe, UK). Their median particle sizes ranged from 0.45 to 4 μm. Native maize starch (CERESTAR UK Ltd., C*03401) was used as the binder and pore former, while poly-acrylic acid, (Allied Colloids Ltd., Dispex A40), was used as a dispersant. Further details of the materials used in this work are listed in Table 1. Prior to mixing, all powders including starch were dried at 120 °C for 24 h.

Based on previous studies [7,22], the slip total solids-loading was set to 59.1 volumetric per cent. The first variable was the starch content and this was incremented in 10% volumetric steps of the solids loading. A second variable was the alumina powder particle size. Slip batches of 500 g solids were prepared. The alumina and starch density values used in the slip formulation were 3.98 g/cm^3 and 0.56 g/cm^3, respectively. Ball milling for 24 h at 66 rpm using spherical alumina grinding media ranging from 5 to 15.5 mm in diameter followed. In order to avoid air entrainment, the ceramic slips were vacuum de-gassed before forming.

The ceramic slips were poured into aluminium moulds and heated in an air circulating oven at 65 °C. Forming time was typically 1 h. After consolidation, the castings were de-moulded without any significant deformation and then dried for 24 h at 120 °C prior to sintering.

The furnace cycle included binder burnout, pre-sintering and sintering steps carried out in 1 integrated operation. The equipment used was a box furnace fitted with a 0.1 °C resolution controller. The starch granules were burned out at a slow heating rate of 1 °C/min up to 500 °C, with 1 h holds at 200 and 300 °C. Binder burnout was previously [25] validated on a number of specimens by mass and dimensional measurements, at interrupted stages of the furnace cycle. The pre-sintering and sintering operations were conducted within a similar heating rate observing temperature holds of 1 h at 1000 °C and 2 h at 1550 °C, respectively. These conditions were kept constant throughout the research.

The disc shaped specimens produced were near net shape. However, grinding was used to remove the casting's "skin" and to produce precise dimensions whilst providing flat and smooth surfaces similar to those required for precision porous aerostatic bearings. Conventional grinding machines, i.e. surface grinder for parallel surfaces and universal for cylindrical grinding were used. Grinding wheels used were high concentration diamond

Fig. 1. Porous ceramic aerostatic structures produced using the starch consolidation technique.

grit, typically D107-100. Roughness typically achieved was in the order of 1 μm Ra. This was characterised using a form Talysurf L120 (Taylor Hobson Ltd.). Ground specimens were cleaned of all loose debris by immersion in an ultrasonic bath of isopropanol for 15 min. The specimens were then dried at 120 °C for 24 h. Fig. 1 illustrates some of the porous aerostatic specimens produced.

3.2. Measurement of porosity and density

Porosity and density measurements were conducted on ground specimens using a modified version of BS EN ISO 2738 [26]. Initial work [5] found the submersion method recommended by the standard procedure for specimen impregnation, resulted in large closed porosity volume, particularly on smaller pore bearings. The modified procedure closely resembles EN 623-2 [27] and enables improved impregnation by evacuating dried specimens before water submersion and repressuration. Further details of the procedure and its validation for sintered alumina porous ceramics have been previously presented by Kwan [28]. The procedure essentially consists of weighing the porous specimens dried, fully impregnated while suspended in water, and finally free standing while impregnated. From these data, open and closed porosity, bulk density and volume of pores were calculated by the methods described in the modified standard [28].

Water impregnation of the specimens was conducted in a chamber. Evacuation time was set to a minimum of 15 min at a typical vacuum pressure of 2.4 kPa [28], followed by immersion until all bubbling stopped. Weighing was conducted using an electronic balance with a 1μg resolution. A value of 3.98 g/cm^3 was used for the theoretical full density of alumina.

3.3. Dimensional shrinkage and process densification

Dimensional shrinkage was calculated for selected specimens using Eq. 1. Measurement of the diameter, thickness and mass was conducted before and after sintering to establish their densification from green state to sintering. The diameter was measured on 5 different locations using a digital calliper. Similarly, the thickness was determined by taking 8 measurements at different locations around the diameter. The mass of the specimens was measured using an electronic balance with a 1 μg resolution.

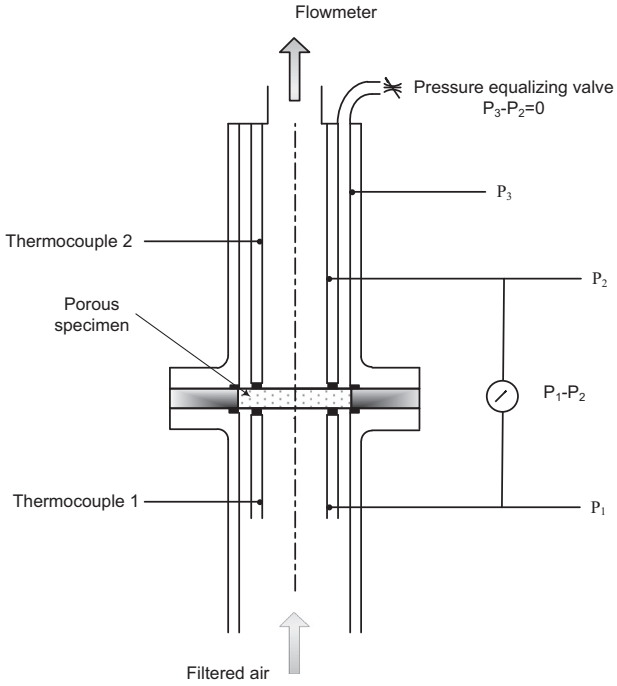

Fig. 2. Permeability measurement schematic.

Densification (δ) was defined as the change in density from green state divided by the maximum possible density change:

$$\delta = \frac{\rho_s - \rho_g}{\rho_t - \rho_g} \tag{12}$$

where ρ_t is the theoretical density for the alumina, ρ_s is the sintered density and ρ_g is the green density.

3.4. Measurement of permeability

The permeability of the porous ceramic specimens was measured using a specially designed test rig compliant with standard BS 5600 [11]. A schematic of this equipment is shown in Fig. 2.

Prior to the permeability measurements, the specimens were dried at 120 °C for 24 h, and kept in a desiccator. Each specimen was held to an aluminium carrier that served as an outer-edge seal, as well as locating datum. During measurement, compressed air was used as the test fluid. Dried and filtered air was supplied to the rig via a computer controlled pneumatic regulator. Air flowed across the disc shaped specimen and was ejected at the top of the rig. A flow metre, several pressure sensors and thermocouples were used to monitor and capture the pressure drop across the bearing along with the volumetric flow rate, the air temperature, ambient pressure and temperature. The test rig incorporated a concentric tube arrangement to minimise edge losses by equalising the

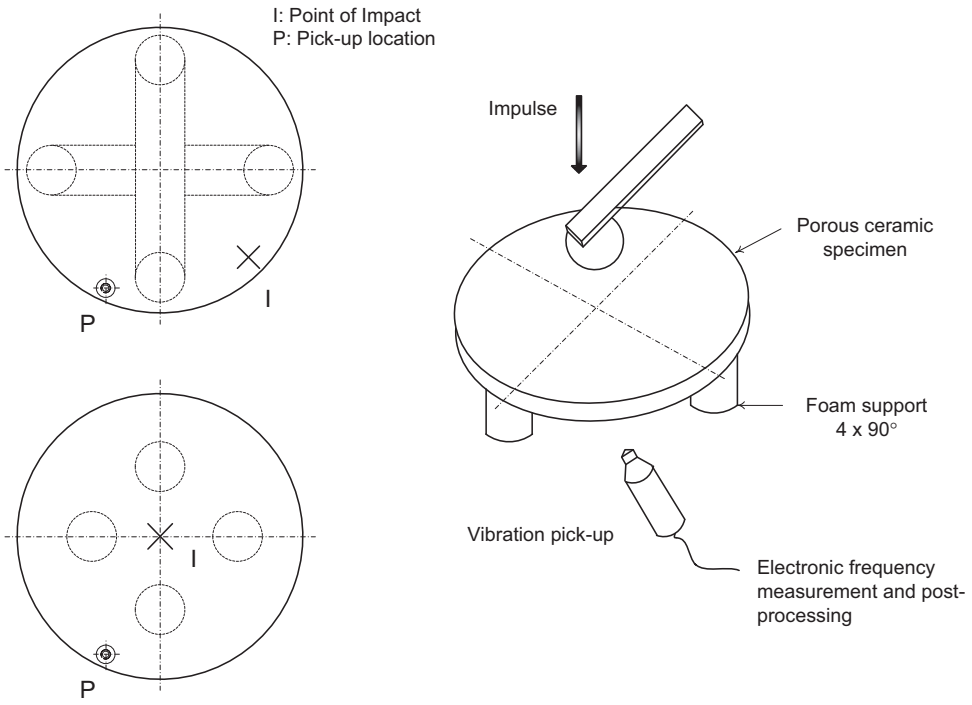

Fig. 3. Schematic of elastic moduli measurement.

pressure in the inner and outer chambers. The pressure differential across the bearing ranged from 75 kPa to 500 kPa. Typically between 12 and 18 readings were taken. At least 1 min was allowed after each pressure increment to ensure steady state flow.

3.4.1. Microstructure and pore size distribution

Pore characteristics and distribution was assessed by a combination of adjunct techniques: bubble test [29], water expulsion method [30] and scanning electron microscopy (SEM). Both, bubble test and the water expulsion method were used to characterise pores that correspond to the equivalent connecting contact areas or necks.

The test rig used for permeability measurements was adapted to conduct these 2 pore characterisation tests. Specimens fully impregnated with deionised water were used in both. For the bubble test, the specimens were positioned in the test rig and were further covered with a column of water of known height. Pressurised air was gradually passed through the specimen from opposite side of the water column. The recorded value of the pressure at which the first bubble emerges on the top surface, was used to calculate the maximum equivalent capillary diameter of the pore, in agreement with the methods detailed in standard procedure [29].

In the water expulsion method, the air pressure fed to the impregnated specimen is gradually increased until it overcomes surface tension of water in the largest pore. Water is then expelled initiating air flow across the specimen wall. As the supplied air pressure is increased, more water is expelled from an increasing number of pores of decreasing size. The pressure difference P_0 and volume flow Q across the specimen are both monitored throughout the procedure. For each pressure increment, the equivalent pore size corresponding to the resulting differential pressure and the number of pores contributing to the corresponding airflow increment were calculated using Gelinas et al. method [30]. Successful characterisation of the pore size distribution using water expulsion for porous ceramic structures has been reported before [4,7].

SEM analysis conducted was on sintered specimens and was primarily concerned with the overall pore structure formed by the voids left by starch particles. From a selection of specimens, 1 centre section was sliced to expose a porous wall surface layer. These sections were mounted in resin and progressively polished using a fine diamond suspension on hard cloth. Following preparation, a series of micrographs was taken.

3.5. Measurement of elastic moduli

The elastic moduli of the specimens, Elasticity and Shear, were measured on disc specimens using the impulse excitation technique [31]. This technique is based on the analysis of the specimen's transient natural vibration resulting from mechanical impact. The moduli are estimated using the specimen's mass, its dimensions and the resulting resonance frequency. A great advantage of this method is that it is non-destructive.

A Lemmens GrindoSonic Mk5 machine was used. This machine calculates Young's modulus using [32]:

$$f_{mn} = \lambda_{mn} \frac{h}{R^2} \left(\frac{X}{12\rho(1-\upsilon^2)} \right)^2 \tag{13}$$

where f_{mn} is the general expression for the transverse vibration frequency of a circular plate of constant thickness (h). R is the

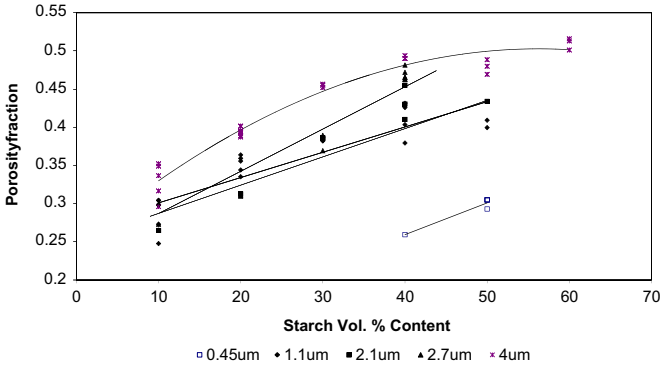

Fig. 4. Porosity dependence on starch vol%.

Table 2
Porosity-starch best-fit line constants by alumina size.

Alumina median size (μm)	m	b	R^2
0.45	0.007	−0.027	0.88
1.1	0.005	0.25	0.97
2.1	0.006	0.19	0.99
2.7	0.007	0.19	0.96
4	0.006	0.28	0.96

specimen radius, ρ is its density, X is Young's modulus and υ is Poisson's ratio. λ_{mn} is a dimensionless coefficient which is a function of the boundary conditions, h/R ratio and υ.

Shear modulus can be obtained from:

$$G = \frac{X}{2(1+\upsilon)} \tag{14}$$

G is the shear modulus. The full details of the moduli calculation can be found elsewhere [33].

Fig. 3 shows a schematic of the measurement procedure. During measurement, each specimen was supported on a thin piece of foam material of very low stiffness. The specimen was then struck at selected nodal points with a 4 mm hardened steel ball, bonded to the end of a flexible plastic strip. The response was measured by a piezo-electric probe placed on the specimen's diameter.

4. Results and discussion

4.1. Specimens porosity

Porosity measurements were conducted on 60 specimens comprising the full range of slip formulations. Results are shown in Fig. 4. The fractional porosity of the specimens ranged from 0.24 to 0.51. Porosity was clearly influenced by both the amount of starch and the alumina powder size. Generally, increasing the amount of starch resulted in greater porosity levels. The increasing number of starch granules leaves an increasing number of pores in the ceramic matrix after binder burnout and sintering. Conversely, lower starch amounts results in lower porosity. Similar behaviour has been reported by others [23,24]. In general, closed porosity was much lower than 1% of the total porosity and was considered negligible.

The same divergence previously observed on SC hydrostatic journal bearings [7] was observed for the larger alumina specimens at starch contents over 40% vol. The porosity of these specimens did not increase linearly, but remained at approximately the same level observed at 40 vol%, showing wider data scattering. This phenomenon has been attributed to minor breakdown of the starch particles during the consolidation stage, resulting in smaller, unstable pores excluded during the sintering operation [22].

The best-fit lines describing the effect of starch on porosity for each alumina size were of linear form:

$$\xi = mS_v + b \tag{15}$$

where ξ is the specimen fractional porosity, m is a coefficient related to the particle size, b is a constant and S_v is the starch solids volumetric %. The empirically derived constants for each alumina particle size are presented in Table 2. These are in close agreement with those of previous research [7]. This suggests that the manufacturing method is consistent regardless of the components shape and their permeability requirement.

As seen, the porosity-starch content trend-lines for each alumina size showed comparable slopes. The smaller alumina particle sizes had higher y-axis intercept, and vice versa. This effect is mainly attributable to the sintering characteristics of each alumina particle size at the selected sintering conditions, as previously noted [7]. Alumina powders of 0.45 μm in size typically approach full density following the sintering conditions used, and its data trend-line reflected this. Previous research [7] showed alumina powders of this size with starch contents below 40% produced dense structures of low permeability for porous aerostatic applications. Therefore, processing of 0.45 μm alumina specimens at these lower starch contents was not further pursued.

In agreement with previous research [7], it was observed that the porosity of the SC porous aerostatic pads was first influenced by the sintering rate of the alumina size used at the chosen sintering conditions. A second influence was the addition of starch, which can increase the porosity a further 20–25%, depending on the size of the alumina used. The former had a stronger influence at the lower starch contents, while latter's influence became more evident at the higher starch contents [7].

4.2. Dimensional shrinkage and densification

Initial results showed that for specimens made with alumina powders ranging from 1.1 to 4 μm, the amount of starch did not significantly influence shrinkage. For these specimens, the size of alumina the powder only had a moderate influence. Shrinkage ranged from 0.05 to 0.08 with that of the smaller alumina powders sizes being marginally higher. In contrast, Shrinkage was significantly larger for the 0.45 μm alumina specimens; typically of 0.15. However, the data set produced was not large enough to observe a trend.

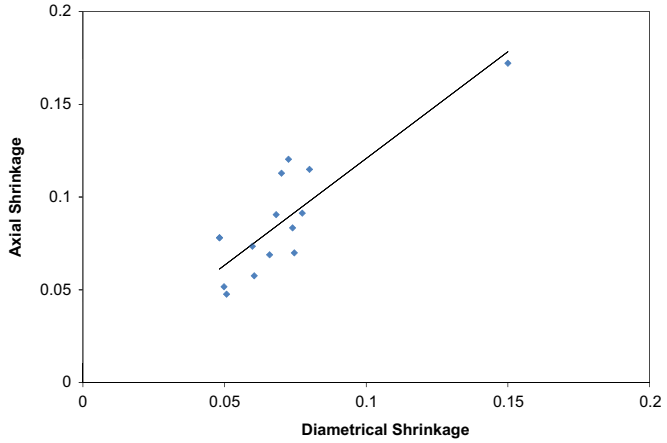

Fig. 5. Porous specimens axial vs. diametrical shrinkage correlation. Plot shows combined data for 14 specimens which alumina powder size ranged from 0.45 to 4 μm. Starch vol. content ranged from 10% to 40%.

For the pad bearings produced, shrinkage was generally of isotropic nature and a good correlation between the diametrical and the axial shrinkages was observed as shown in Fig. 5. This suggested good uniformity across the ceramic matrixes; and therefore uniformity and consistency of the casting physical properties, such as permeability. These are important for porous aerostatic applications to ensure uniform and smooth relative motion. Some validation of microstructural uniformity was established in previous research [25] by measuring the density (Section 3.2) of longitudinally and circumferentially sliced segments of large porous SC alumina specimens.

Results also showed that, with the exception of the 0.45 μm alumina specimens, shrinkage of all other specimens was comparable. Neither the vol% of starch nor the individual sintering rate of the alumina powders had an apparent dominant influence. Shrinkage was significantly larger for the 0.45 μm alumina. The differing behaviour is attributable to the chosen sintering conditions that resulted in similar, less-advanced stages of sintering for the specimens made with alumina powders ranging from 1.1 to 4 μm. Previous SEM images [7] showed that smaller alumina had indeed achieved more advanced sintering stages using similar sintering conditions.

The relationship between shrinkage and densification was generally observed to have a reasonable correlation with the values obtained via Eqs. (2) and (12), particularly on specimens having porosity ≤ 0.38. As shown in Fig. 6, experimental data showed good convergence with the predicted. Some divergence was noticeable for specimens having porosity ≥ 0.41, with the densification always being lower than predicted. For these specimens, a more accurate relationship was found by curve fitting the experimental data, resulting in a linear equation of the form:

$$\delta = 1.76\frac{\Delta L}{L_0} - 0.0276 \tag{16}$$

where δ is densification (fraction, dimensionless) ΔL is the compact length change from sintering, L_0 is the initial compact

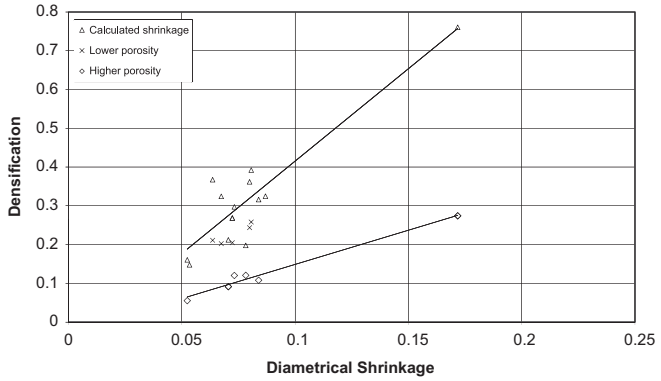

Fig. 6. Relationship between calculated and measured shrinkage vs. densification.

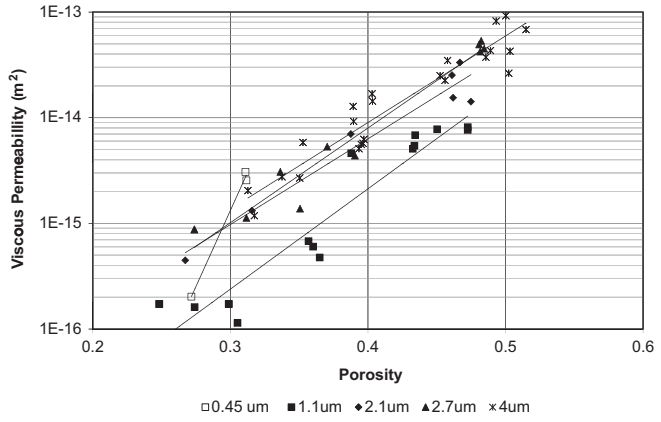

Fig. 7. Porosity dependence of viscous permeability for SC porous aerostatic specimens.

length. However, curve fitting was produced with a relatively small data set; and therefore further measurements need to be conducted for validation. The observed divergence of δ may be attributable to the accumulation of voids noted at the higher starch contents [7], causing disruption of the ceramic matrix densification.

4.3. Permeability and microstructure

Fig. 7 shows the viscous permeability coefficient as a function of porosity. This ranged from 1.55×10^{-16} to 1.04×10^{-13} m^2. Permeability was predominantly viscous and was clearly influenced by the porosity. Generally, increasing of the ceramic slip volumetric starch content resulted in more porous and permeable structures for all alumina sizes. Higher porosity also resulted in larger average pores; and consequently, a larger number of flow interstices within the porous structures. The porosity corresponding to the lowest permeability correlates well with that required for percolation, obtained using the largest equivalent pore [7] (0.30 vs. 0.31).

The porosity-permeability empirical relationship was described by best fit equations of the form:

$$\Psi = k\xi^a \tag{17}$$

where ψ is the viscous permeability coefficient in m^2, k is an alumina powder size empirical constant, ξ is the porosity

Table 3
Porosity-permeability best fit line empirical constants by alumina size. 2nd and 3rd columns from the left show the constants derived in the current research.

Alumina powder size (μm)	k	a	Ref [3]	
			k	a
0.45	1.64×10^{-5}	19.27	–	–
1.1	2.73×10^{-12}	7.70	1.63×10^{-12}	4.81
2.1	4.08×10^{-12}	6.90	–	–
2.7	1.24×10^{-11}	7.85	–	–
4	1.25×10^{-11}	7.80	1.99×10^{-12}	5.15

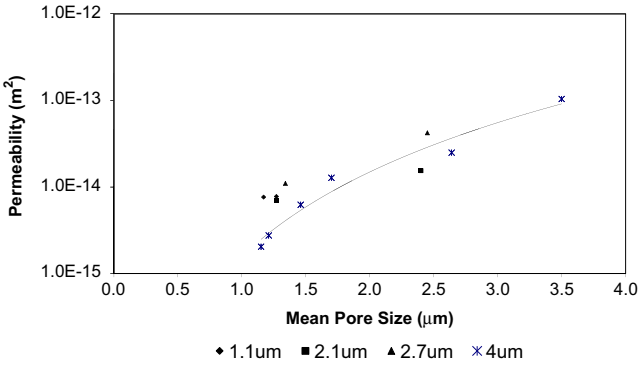

Fig. 8. Effect of the pore size on permeability.

fraction and a is an empirical constant. The trend-lines of the larger alumina powders had higher y-axis intercepts, and vice versa. Table 3 illustrates the constant values for all alumina powders. Equations of the same form were used in previous porous-ceramic aerostatic bearing work [3,5].

The equivalent mean pore diameter ranged from 1.15 to 3.5 μm. In general, for all alumina sizes, an increment of the starch volume resulted in larger pores. This was an effect of the increasing number of voids left by the starch particles. Also, specimens made with larger alumina powders generally resulted in larger pores for a given slip formulation using fixed processing parameters. This was due to the lower sintering rate of these powders, which as observed, resulted in higher porosity too. The same behaviour was noted previously [7]. Conversely, lower porosity specimens showed smaller pores.

The relationship between the pore size and permeability is shown in Figs. 8. For 4 μm alumina specimens, this was expressed using a power law equation (Eq. (5)). As observed, permeability grew rapidly with the size of the average pore. Although the power constant obtained is comparable with that found by Vasconcelos et al. [14] (3.24 vs. 2), the derived coefficient is smaller (1.58×10^{-15} vs. 2.54×10^{-14}). These differences are attributable to the larger size of the potato starch granules (approximately 50 μm), the lower sintering temperature and solids loading used by Vasconcelos et al. [14] that resulted in more permeable compacts.

In view of the pneumatic instability sometimes observed in aerostatic bearings, smaller surface pores are preferred for a given value of the permeability coefficient. Instability is caused by air compressibility, and smaller pores contribute to reduce air volume in the bearing gap.

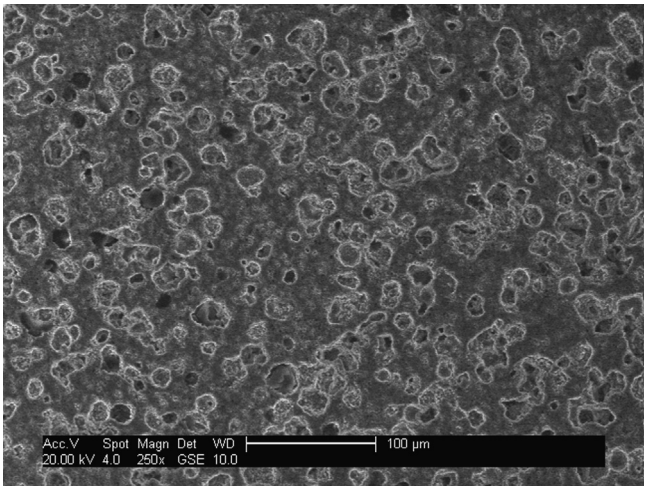

Fig. 9. SEM image of a specimen made with 1.1 μm alumina powders and using a 30% vol starch. Fractional porosity: 0.39, Permeability: 4.61×10^{-15} m^2, Young's modulus: 98 GPa, Shear modulus: 40 GPa.

Fig. 9 shows a SEM image of a porous pad typical microstructure. This was produced using alumina powder of 1.1 μm in diameter and a 30% vol starch. The voids left by the starch particles clearly dominate, with the pores appearing well-dispersed in terms of both distribution and separation, in agreement with previous observations [7]. The pores appear to be of a semi-spherical shape and range from 10 to 20 μm in size, correlating well with the size and shape of the starch granules. The microstructure of other specimens made using 2.1, 2.7 and 4 μm alumina powders with similar slip compositions showed similar distribution and size of the pores. However, specimens made using the smaller 0.45-μm alumina powder showed smaller pores, as reported before [7].

Generally for the same porosity, the permeability of the SC aerostatic porous structures was higher than those produced by injection moulding and slip casting using lower sintering atmospheric temperatures [3]. This was clearly an advantage resulting from the use of starch granules as the pore former. Permeability was also comparable to that achieved by Isobe et al. [34] with specimens having unidirectionally aligned pores.

The permeability range obtained is wider than previously defined for ultra-precision porous aerostatic bearings [5]. This will enable tailoring of permeability to suit a wider range of bearing applications.

4.4. Young's and shear moduli

Young's and shear moduli of over 45 specimens were measured. Young's modulus ranged from 43 to 177 GPa, showing a clear influence of porosity as seen in Fig. 10. Lower porosity specimens showed larger values of Young's modulus. Conversely, large porosity specimens showed lower modulus. All the data points converged well, regardless of the

alumina powder used; when grouped together, a good correlation was still observed.

The shear modulus measurements results are shown in Fig. 11. As with the elastic modulus, a clear influence of porosity can be readily appreciated. A maximum value of 73 GPa was observed at a fractional porosity of 0.25. The shear modulus increased rapidly with a decreasing porosity, and vice versa.

The moduli experimental data were least square fitted with 3 different functions: power, exponential and that derived empirically by Zivcova et al. [21], represented by Eqs. (9)–(11). Table 4 shows the empirically derived constants for both Young's and shear moduli. The power equation appeared to give the most accurate fit. However, all 3 equations showed very good agreement with the measured data, with only very small differences in the sum of square of the relative error. The value of the empirically derived constant X_0 compares to the 410 GPa quoted for Young's modulus of fully dense alumina [35]. The value for the empirical constant a is consistent with the results observed by Wagh [18] for ceramics fabricated without hot pressing or sintering aids ($a \approx 2$).

Kwan et al. [36] and Roach [3] fitted similar curves for porous aerostatic thrust bearings. They obtained constants that are comparable to the ones derived in this research, as shown in Table 4. The differences observed may be in part due to the different pore morphology achieved by the different processing routes employed. This is in agreement with Costa-Oliveira [37] et al. who previously noted some discrepancies in Young's modulus between porous ceramics manufactured with different forming techniques.

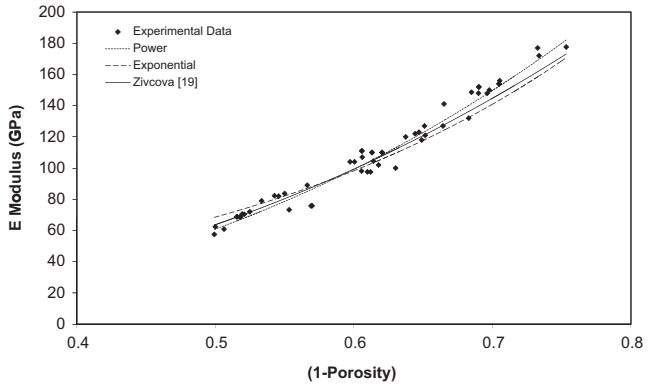

Fig. 10. Effect of porosity on Young's modulus.

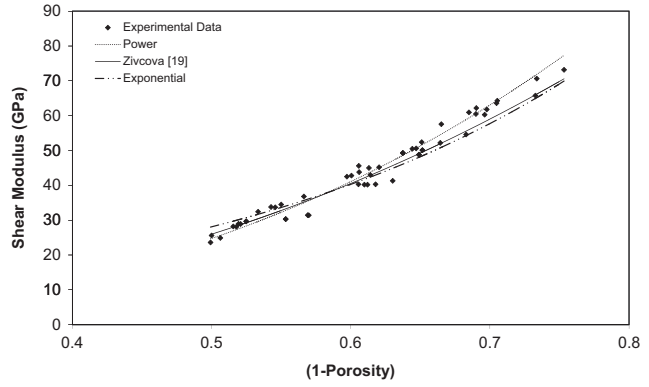

Fig. 11. Effect of porosity on the shear modulus.

Table A1
Specimens made by alumina particle size and slip formulation.

Starch (vol%) / Alumina median size (μm)	10	20	30	40	50	60
	No. of specimens tested					
0.45	–	–	–	**1**	**2**	–
1.1	**4**	**3**	**1**	**4**	**2**	–
2.1	**1**	**1**	**1**	**3**	**1**	–
2.7	**1**	**3**	**2**	**4**	–	–
4	**5**	**8**	**3**	**3**	**3**	**3**

Table A2
Average and range porosity of specimens in Table A1.

Starch (vol%) / Alumina median size (μm)	10	20	30	40	50	60
	Average porosity/range					
0.45	–	–	–	**0.27/–**	**0.31/ 0.006**	–
1.1	**0.28/ 0.057**	**0.36/ 0.008**	**0.39/–**	**0.44/ 0.018**	**0.47/ 0.000**	–
2.1	**0.27/–**	**0.32/–**	**0.39/–**	**0.46/ 0.006**	**0.47/–**	–
2.7	**0.27/–**	**0.33/ 0.039**	**0.38/ 0.020**	**0.48/ 0.004**	–	–
4	**0.33/ 0.040**	**0.40/ 0.014**	**0.46/ 0.005**	**0.50/ 0.007**	**0.49/ 0.018**	**0.51/ 0.015**

Table 4
Elastic moduli empirical constants.

	$X = X_0(1-\xi)^a$ [18]		$X = X_0 e^{-b\xi}$ [19,20]		$X = X_0 \cdot [(1-\xi)^2/(1+\xi)]$ [21]
	X_0	a	X_0	b	X_0
Modulus of elasticity (GPa)	**388**	**2.67**	**415**	**3.6**	**385**
Shear modulus (GPa)	**170**	**2.78**	**170**	**3.6**	**157**
Kwan [36] Modulus of elasticity (GPa)	**479.7**	**3.91**	**576.1**	**5.38**	–
Kwan [36] Shear modulus (GPa)	**193**	**3.82**	**230.8**	**5.26**	–
Roach [3] Modulus of elasticity (GPa)	**276**	**4.11**	**464**	**6.62**	–
Roach [3] Shear modulus (GPa)	**135**	**4.38**	**234**	**7.05**	–

Table A3
Average and range permeability of specimens in Table A1.

Starch (vol%) Alumina median size (μm)	10 Permeability average/range (m^2)	20	30	40	50	60
0.45	–	–	–	2.03E-16/–	2.81E-15/5.15E-16	–
1.1	1.55E-16/5.85E-17	5.85E-16/2.03E-16	4.62E-15/–	6.28E-15/2.69E-15	7.89E-15/4.93E-16	–
2.1	4.47E-16/–	1.31E-15/–	7.10E-15/–	2.47E-14/1.79E-14	1.61E-14/–	–
2.7	8.75E-16/–	1.86E-15/1.95E-15	4.85E-15/9.46E-16	4.75E-14/1.11E-14	–	–
4	2.90E-15/4.65E-15	8.68E-15/1.39E-14	2.74E-14/1.21E-14	9.28E-14/2.18E-14	4.11E-14/5.76E-15	4.73E-14/4.19E-14

Table A4
Pore and permeability raw data used to characterise the effect of the pore size on permeability.

Specimen no.	Alumina size (μm)	Starch (vol%)	Pore size (μm)		V Perm (m^2)
			Mean	Max	
111	1	40	1.27	3.78	7.77E-15
111	1	50	1.17	2.28	7.65E-15
111	2	30	1.27	2.77	7.01E-15
211	2	40	2.40	5.62	1.54E-14
111	3	30	1.34	3.76	1.10E-14
411	3	40	2.45	5.60	4.23E-14
111	4	10	1.15	2.84	2.04E-15
211	4	10	1.21	3.25	2.76E-15
212	4	20	1.70	5.64	1.28E-14
412	4	20	1.46	4.52	6.24E-15
411	4	30	2.64	7.50	2.49E-14
411	4	40	3.50	7.37	1.04E-13

Overall, the elastic moduli results are well within the range of porous aerostatic applications. They are consistent with those obtained by of Zivcova et al. [21], comparable with the results of by Kwan et al. [36], and generally higher than the results obtained by Roach [3], at similar porosities. The SC alumina porous bearings have been sintered at a higher temperature (1550 °C) than that used by Roach [3], leading to stronger bonds. The pores created by the starch granules contribute to achieve the functional bearing porosity without compromising their structural properties.

Porous structures made of alumina that are potentially suitable for aerostatic porous bearings were successfully produced using the SC technique. Aerostatic circular pads produced with this technique exhibited well-defined, reliable, and reproducible permeability with robust elastic properties.

Numerous previous SC technique publications tend to focus on the processing of submicron alumina powders. The present research expands the scope of this by employing a range of alumina powders of up to 4 μm.

The scope of this work does not include performance testing of aerostatic bearings made with SC technique. Important performance aspects such as the effect of bearing surface pore-structure on stability need to be investigated for validation. This will be part of a separate programme.

5. Conclusions

- The required permeability range for aerostatic bearing applications, 3.13×10^{-15}–8.44×10^{-14} m^2, was successfully achieved, with a fractional porosity ranging from 0.32 to 0.48. The mean pore size calculated by the water expulsion method ranged from 1.23 to 1.5 μm.
- A desired Young's modulus of 102 GPa for an aerostatic ultra-precision pad of 40 mm in diameter and thickness of 6 mm, observing a maximum deflection of 1 μm at pressure drop of 0.17 MPa was obtained at a fractional porosity value of 0.39. Lower porosity yielded higher Young's modulus.
- Both, permeability and elastic moduli were deeply influenced by porosity, which was a function of the alumina powder size and the amount of starch used.
- The use of starch as binder and pore former, coupled with higher sintering temperatures (1550 °C) enabled systematic control of the porosity without compromising the elastic properties.

Appendix A

See Tables A1–A4 here.

References

[1] F. Levassort, J. Holc, E. Ringgaard, T. Bove, M. Kosec, M. Lethiecq, Fabrication, modelling and use of porous ceramics for ultrasonic transducer applications, J. Electroceram. 19/1 (2007) 125–137.
[2] M. Takahashi, R.L. Menchavez, M. Fuji, H. Takegami, Opportunities of porous ceramics fabricated by gelcasting in mitigating environmental issues, J. Eur. Ceram. Soc. 29/5 (2009) 823–828.
[3] C.J. Roach, Development of porous ceramic air bearings (PhD Thesis), Cranfield University, Cranfield, United Kingdom, 2001.
[4] Y.B.P. Kwan, D.J. Stephenson, J.R. Alcock, Dependence of pore size distribution on porosity in hot isostatically pressed porous alumina, J. Porous Mater. 8 (2) (2001) 119–127.
[5] Y.B.P. Kwan, Processing and fluid flow characteristics of hot isostatically pressed porous alumina for aerostatic bearing applications, PhD Thesis, Cranfield University, Cranfield, United Kingdom, 1996.
[6] T.H. Panzera, J.C. Rubio, C.R. Bowen, P.J. Walker, Microstructural design of materials for aerostatic bearings, Cem. Concr. Compos. 30/7 (2008) 649–660.

[7] I.S. Durazo-Cardenas, D.J. Stephenson, J. Corbett, Controlled porosity alumina structures for ultra-precision hydrostatic journal bearings, J. Am. Ceram. Soc. 93 (11) (2010) 3671–3678.
[8] R.M. German, Powder Metallurgy Science, Metal Powder Industries Federation, Princeton, NJ, 1984.
[9] Y.B.P. Kwan, J. Corbett, Porous aerostatic bearings-an updated review, Wear 222 (2) (1998) 69–73.
[10] P.R.K. Murti, Analysis of externally pressurised gas porous bearings, J. Lubr. Tech., Trans. ASME series F 96/3 (1974).
[11] British Standards Institution, Powder Metallurgical Materials and Products Part 3. Methods of testing sintered materials-determination of fluid permeability, BS5600, British Standards Institution, 1988.
[12] R.M. German, Porosity and particle size effects on the gas flow characteristics of porous metals, Powder Technol. 30 (1) (1981) 81–86.
[13] E.M. Cliffel, J.,W.E. Smith, A.D. Schwope, Theory and applications of controlled permeability, in: H. Hausner (Ed.), Modern Developments in Powder Metallurgy, Springer, US, 1966, pp. 114–128.
[14] P.V. Vasconcelos, J.A. Labrincha, J.M.F. Ferreira, Permeability of diatomite layers processed by different colloidal techniques, J. Eur. Ceram. Soc. 20 (2) (2000) 201–207.
[15] W.C. Young, Roark's Formulas for Stress and Strain, 6th ed., McGraw-Hill, New York, 1989.
[16] W. Pabst, E. Gregorová, G. Tichá, Elasticity of porous ceramics–A critical study of modulus-porosity relations, J. Eur. Ceram. Soc. 26 (7) (2006) 1085–1097.
[17] K.K. Phani, S.K. Niyogi, Elastic modulus-porosity relationship for Si_3N_4, J. Mater. Sci. Lett. 6 (5) (1987) 511–515.
[18] A.S. Wagh, R.B. Poeppel, J.P. Singh, Open pore description of mechanical properties of ceramics, J. Mater. Sci. 26 (14) (1991) 3862–3868.
[19] Discussion of Ryshkewitch Paper by Winston Duckworth*, J. Am. Ceram. Soc. 36 (2) (1953) 68–68.
[20] R.M. Spriggs, Expression for effect of porosity on elastic modulus of polycrystalline refractory materials, particularly aluminum oxide, J. Am. Ceram. Soc. 44 (12) (1961) 628–629.
[21] Z. Živcová, M. Černý, W. Pabst, E. Gregorová, Elastic properties of porous oxide ceramics prepared using starch as a pore-forming agent, J. Eur. Ceram. Soc. 29 (13) (2009) 2765–2771.
[22] O. Lyckfeldt, J.M.F. Ferreira, Processing of porous ceramics by starch consolidation, J. Eur. Ceram. Soc. 18 (2) (1998) 131–140.
[23] E. Gregorová, W. Pabst, Porosity and pore size control in starch consolidation casting of oxide ceramics–achievements and problems, J. Eur. Ceram. Soc. 27 (2–3) (2007) 669–672.
[24] M.E. Bowden, M.S. Rippey, Porous ceramics formed using starch consolidation, Key Eng. Mater. 213 (3) (2001) 1957–1960.
[25] I.S. Durazo Cardenas, Development of porous-ceramic hydrostatic bearings (PhD), Cranfield University, Cranfield, UK, 2003.
[26] British Standards Institution, Sintered metal materials, excluding hard-metals–permeable sintered metal materials–determination of density, oil content and open porosity, BS EN ISO 2738:2000, British Standards Institution.
[27] British Standards Institution, Advanced technical ceramics-Monolithic ceramics-General and textural properties-Part 2: Determination of density and porosity, BS EN 623-2:1993, British Standards Institution, 1993.
[28] Y.B.P. Kwan, J.R. Alcock, The impact of water impregnation method on the accuracy of open porosity measurements, J. Mater. Sci. 37 (2002) 2557–2561.
[29] British Standards Institution, Permeable sintered materials–determination of the bubble test pore size, BS EN 24003:1993 (ISO 4003: 1977), British Standards Institution.
[30] C. Gelinas, R. Angers, Improvement of the dynamic water-expulsion method for pore size distribution measurements, Am. Ceram. Soc. Bull. 65 (9) (1986) 1297.
[31] J.W. Lemmens, Impulse Excitation: a technique for dynamic modulus measurement, in: A. Wolfenden (Ed.), Dynamic Elastic Modulus Measurements in Materials, American Society for Testing and Materials, Philadelphia, 1990, pp. 90–99.
[32] J.C. Glandus, F. Platon, P. Boch, Measurement of the elastic moduli of ceramics, Mater. Eng. Appl. 1 (6) (1979) 243–246.
[33] J.C. Glandus, Rupture Fragile et resistance aux chocs thermiques de ceramiques a usages mecaniques (PhD), L'Universite de Limoges, Limoges, France, 1981.
[34] T. Isobe, Y. Kameshima, A. Nakajima, K. Okada, Y. Hotta, Gas permeability and mechanical properties of porous alumina ceramics with unidirectionally aligned pores, J. Eur. Ceram. Soc. 27 (1) (2007) 53–59.
[35] R. Morrell, Handbook of Properties of Technical and Engineering Ceramics, 1st. ed, HMSO, London, 1987.
[36] Y.B.P. Kwan, D.J. Stephenson, J.R. Alcock, Porosity dependence of flexural modulus and strength for capsule-free hot isostatically pressed porous alumina, J. Mater. Sci. 35 (5) (2000) 1205–1211.
[37] F.A. Costa-Oliveira, The influence of forming methods on the flexural strength of a porous cordierite-based ceramic, in: Proceedings of the Fourth Euro Ceramics, vol. 1, Basic Science-Developments in Processing of Advanced Ceramics-Part 1, 1995, pp. 389–396.